Article:

Ten implementations of ptychography

Ten implementations of ptychography

Peng Li* and Andrew M. Maiden

Dept. Electronic and Electrical Engineering, University of Sheffield, Sheffield, UK, S1 3JD.
peng.li.shef@sheffield.ac.uk

Abstract: Ptychography is an increasingly popular phase retrieval imaging technique, able to routinely deliver quantitative phase images with extended field of view at diffraction limited resolution. Different variants of this technique, like Bragg ptychography and Fourier ptychography, have also been developed and applied to various fields. Here we experimentally demonstrate 10 ways to implement the conventional real space transmission ptychography, and compare their properties to provide a guide to choosing the optimal setup for a specific application.

Key words: Ptychography; Phase retrieval; Diffuser.

1. INTRODUCTION

When it was first proposed as a lensless imaging alternative for electron microscopy in the 1970s (Hoppe, 1969; Hoppe & Strube, 1969; Hoppe, 1969; Hegerl & Hoppe, 1970; Hegerl & Hoppe, 1972), ptychography could only be applied to crystalline objects, thanks to the constrained set of interference phenomena that can occur in this case. It was not until 1989 when Bates and Rodenburg proposed a direct (non-iterative) reconstruction algorithm called the Wigner distribution deconvolution method (WDDM) (Bates & Rodenburg, 1989), that ptychography became applicable to amorphous objects. However, WDDM still requires the specimen to be scanned over a grid of 2D positions separated by the desired resolution in the final reconstruction and a 2D diffraction intensity to be recorded at each scan position, which gives rise to a very large 4D data set. The 4D data set, however, can be substantially reduced by using fewer and bigger detector pixels when the sample satisfies the weak phase approximation (McCallum *et al.*, 1995; Yang *et al.*, 2015; Brown *et al.*, 2016). A breakthrough in ptychography was made when iterative algorithms were used to solve for the phase problem in 2004 (Faulkner & Rodenburg, 2004; Rodenburg & Faulkner, 2004). Since

then, further algorithmic developments have made ptychography a very powerful and useful imaging technique. Alongside the object function, the illumination function (Guizar-Sicairos & Fienup, 2008; Thibault *et al*., 2009; Maiden & Rodenburg, 2009), the scan positions (Maiden *et al*., 2012; Zhang *et al*., 2013; Tripathi *et al*., 2014) and the partial coherence (Thibault & Menzel, 2013) can also be recovered from the dataset. In addition, ptychography can image 3D objects via the multislice method (Maiden *et al*., 2012) or via the combination of tomography (Dierolf *et al*., 2010). It has also been modified to operate in a Bragg geometry (Godard *et al*., 2011) and adapted to eliminate the mechanical scan of the specimen via Fourier Ptychography (Zheng *et al*., 2013) where the roles of real and reciprocal space are interchanged and the 'scanning' is carried out by illumination tilts.

The ptychographic imaging process is illustrated in Fig. 1a. There are three fundamental components: a confined probe, an overlapping scan strategy and an iterative image reconstruction algorithm. The confined probe can be formed by passing an extended beam through a pinhole or by condensing the extended beam via a lens. In either case, a diffuser (a randomly scattering medium) can also be inserted to increase the angular range of the probe, giving rise to the four probe-forming methods illustrated in Fig. 1b. (In what follows, the four methods will be referred to according to their numbering in Fig. 1b.) It should be noted that although a probe can also be formed by imaging a pinhole (or a pinhole with a diffuser) via a 4f system (Maiden *et al*., 2012), this is essentially the same as probe 3 (or probe 4) in Fig. 1b.

Ptychography makes measurements of multiple diffraction patterns via an overlapping scan strategy, where the illuminated areas from two adjacent scan positions partially overlap. Provided this overlap is sufficient, the redundancy it introduces allows iterative algorithms to re-phase the measurements and reconstruct complex images of the specimen and the probe. These algorithms broadly follow the block diagram shown in Fig. 1c, although there are

many variants on how each block in the diagram is implemented; we will use the ePIE algorithm (Maiden & Rodenburg, 2009) throughout this paper.

Although invented to circumvent the need for lenses, ptychography can also be implemented with their assistance. There are three possible setups (the variant Fourier ptychography is not considered here). We will refer to the configuration with no lenses in between the specimen and the detector as the 'lensless setup' (see Fig. 2a). This is the most common form of ptychography and it is very popular in the x-ray community (Thibault *et al.*, 2008). An alternative configuration using a microscope imaging system (an objective lens and a tube lens) to image near-field diffraction patterns has been demonstrated in the visible light regime (Godden *et al.*, 2014); we refer to this setup as the 'microscope setup' because of its similar appearance to a microscope. Another approach is the 'selected area setup', which has been demonstrated using visible light (Maiden *et al.*, 2012) and also in electron microscopy (Maiden *et al.*, 2015), where the objective lens images the specimen onto a selected area aperture and the resulting wavefront forms a near-field diffraction pattern on a detector. Compared to the lensless setup, in the microscope setup the detector is replaced with its demagnified image (see Fig. 4a) and in the selected area setup the specimen is replaced with its magnified image (see Fig. 7a).

Combined with the four probe types, the three imaging setups can give rise to ten ways to implement ptychography (since for the selected area setup, plane wave illumination is needed, so probes 3 and 4 cannot be used). Our objectives in this paper are to demonstrate these ten different configurations using visible light experiments, to compare their performance, and to assess the advantages and disadvantages of each approach.

2. EXPERIMENTS

For each of the ten different configurations, we carried out a ptychographic experiment on a microscope slide of moss antheridium (see Fig. 2d) using a 635nm laser diode source. For each experiment, the ptychographic scans consisted of a 15×15 raster grid of specimen positions with a nominal 20µm step size, plus ±20% random offsets to the grid to avoid reconstruction artefacts. In the experiments, the aperture used to form probe types 1 and 2 had a diameter of 100µm and the lens chosen to form probe 3 and probe 4 had a focal length of 35mm. The NA of the lens was about 0.17. The diffuser used in probe 2 and probe 4 was a piece of plastic film. The 16-bit CCD detector used to record the diffraction patterns had 2048×2048 pixels with a pitch of $7.4µm^2$. The recorded diffraction patterns were binned by a factor of 2 to save data processing time and reduce noise.

2.1. The lensless setup

The lensless setup is illustrated in Fig. 2a. The distance from the specimen to the detector was set at 17mm, resulting in a pixel size for the reconstructed specimen image approximately matching the experiments using the other setups. The diffraction patterns that resulted from the four different probes (at the central scan position) are shown in Fig. 2b. As we can see, the aperture on its own (probe 1) produces a bright spot in the centre of the diffraction pattern caused by the unscattered beam. As a result, the scattered beam, especially at high angles, is too weak to be detected with good signal-to-noise ratio because of the limited dynamic range of the CCD. The use of a diffuser or a lens can help mitigate this problem by introducing higher incident angles into the probe illumination. In this case, on comparing the top right and bottom left diffraction patterns in Fig 2b, the higher intensities toward the edges of the bottom left diffraction pattern indicate that the lens introduces a greater range of angles than does the diffuser. When the diffuser and the lens are used together, a much broader region of the CCD can detect significant signals. As a result, this allows us to expect the worst reconstruction from probe 1 and best reconstruction from probe 4.

We used the Fresnel number (Goodman, 2005) as the criteria to determine the propagation

model between the specimen and the detector. The Fresnel number is defined as

$$N_F = \frac{a^2}{\lambda z}, \tag{1}$$

where a is the size of the probe, λ the wavelength of the radiation source and z the distance

of the detector from the specimen. When $N_F \ll 1$, the Fourier propagation (i.e. Fraunhofer

diffraction) should be used; when $N_F \approx 1$, the Fresnel propagation (i.e. Fresnel diffraction)

should be used; and when $N_F \gg 1$, the angular spectrum propagation should be used. Here

the Fresnel number is approximately 0.93, very close to 1, so we used the Fresnel propagation

in the reconstruction. The Fresnel propagation model is given by

$$\Psi(u,v) = FT\left\{ \psi(x,y) \exp\left[\frac{i\pi}{\lambda z}(x^2 + y^2) \right] \right\}, \tag{2}$$

where (x,y) is the coordinate of the specimen plane, (u,v) the coordinate of the detector

plane and FT is the Fourier transform operation. The pixel dimensions $(\Delta x, \Delta y)$ in the

specimen plane are given by

$$\begin{cases} \Delta x = \dfrac{\lambda z}{D_x} \\ \Delta y = \dfrac{\lambda z}{D_y} \end{cases}, \tag{3}$$

where D_x and D_y are the detector dimension along the x and y directions respectively.

Here the pixel size of the reconstructions is about 0.71μm in each direction.

200 iterations of ePIE were run on each data set. The initial object guess was free space, i.e. a

matrix of 1s. The initial probe guess was generated according to the experimental geometry:

for probe 1 and probe 2, the initial guess was just an aperture of approximately the correct

size; for probe 3 and probe 4, the initial guess was a modelled convergent beam with a defocus applied to match that measured from the experimental apparatus. The moduli of the reconstructed probes from each of the four probe types are shown in Fig. 2c. Fig. 2d gives the full reconstructed image from the experiment using probe 4 as an example, whilst Fig. 2e shows zoom-ins of the four object reconstructions from each of the four probe types.

Visually, the reconstruction quality is consistent with the above analysis of the recorded diffraction patterns, with probes 3 and 4 giving much sharper features. To quantitatively assess the reconstruction quality, we used a metric called Fourier ring correlation (FRC) (Van Heel & Schatz, 2005). The FRC calculates the frequency correlation between the results from two independent experiments. High correlation means the information of the corresponding frequency is stably reconstructed, while low correlation implies the information is not reliable. The FRC plot is shown in Fig. 3 and it indicates the same quality trend as that of the visual comparison.

2.2. The microscope setup

The microscope setup, where diffraction data is collected using a conventional microscope followed by a CCD detector, is illustrated in Fig. 4a. Here the microscope used an objective lens with a NA of 0.65 combined with a tube lens of focal length 100mm, giving a calibrated magnification for our system of 21.45. Ignoring lens aberrations, this setup can be viewed equivalently as a lensless setup with a very small virtual CCD, demagnified by the microscope magnification and located at the front focal plane of the objective lens. Since the CCD is much smaller now, the distance from the specimen to the CCD conjugate plane cannot be too big, otherwise signals will be scattered beyond the edges of the virtual detector. Here we set this distance to be 0.5mm, giving diffraction patterns as shown in Fig. 4b. It should be noted that since the virtual CCD plane is at the proximity of the specimen plane,

the resulting diffraction patterns will have a relatively low dynamic range compared to the lensless setup. As a result, the dynamic range of the detector is not a limiting factor anymore and the signals can be detected with high fidelity for all the four probe forming methods. Consequently, it is difficult to predict the reconstruction quality here based solely on the diffraction patterns themselves.

For the reconstruction, the CCD was scaled down to its conjugate plane, which means the detector is demagnified by 21.45. According to the Fresnel number calculation (about 31.5, much bigger than 1), the angular spectrum propagation model is used for the propagation between the specimen and the CCD conjugate plane. The angular spectrum propagation model is given by

$$\psi'(x,y) = FT^{-1}\left\{FT\{\psi(x,y)\}\exp\left[\frac{i2\pi z}{\lambda}\sqrt{1-(\lambda u)^2-(\lambda v)^2}\right]\mathrm{circ}\left(\sqrt{(\lambda u)^2+(\lambda v)^2}\right)\right\}, \quad (4)$$

with

$$\mathrm{circ}\left(\sqrt{(\lambda u)^2+(\lambda v)^2}\right) = \begin{cases} 1, & (\lambda u)^2+(\lambda v)^2 \leq 1 \\ 0, & (\lambda u)^2+(\lambda v)^2 > 1 \end{cases}, \quad (5)$$

where FT^{-1} is the inverse Fourier transform operation. The pixel size of the specimen and the pixel size of the virtual detector are equal because of the two successive Fourier transforms in the angular spectrum propagator. Since the virtual detector is formed by demagnifying the actual detector by 21.45, the pixel size of the reconstructions is equal to $2\times7.4/21.45=0.69\mu m$.

As previously, 200 iterations of ePIE were run on each data set with an initial object guess of free space and an initial probe guess being generated according to the experimental geometry. The reconstructed probes (the modulus part of the central region with significant values) from each of the four probe types are shown in Fig. 4c. Fig. 4d gives the full reconstructed image

from the experiment using probe 4 as an example, whilst Fig. 4e shows zoom-ins of the four object reconstructions from each of the four probe types.

Visually, compared to the results from the lensless setup, the four reconstructions are all very good. Quantitatively, an FRC analysis gives very high correlations for all the methods, compared to those from the lensless setup. But surprisingly, the reconstruction quality trend is opposite to the case of the lensless setup. Since the recorded diffraction patterns all have good enough signal-to-noise ratios, we suspect that the reconstruction quality is more affected by the structure of the probe here. The specimen reconstruction is realized by decoupling the probe from the updated exit wave (see Fig. 1c), meaning the probe structure and the specimen reconstruction are interdependent. If the probe structure is very rough, it will cause similar profile variations in the specimen reconstruction, hence affecting the FRC curve. As shown in Fig. 4c, probe 1 and 2 have rather smooth speckles with big characteristic size, while probe 3 has a bright spot in the centre and ripples, and probe 4 has very small and random speckles. It is obvious, when we plot their cross-sections along the central vertical line in Fig. 6, to see that probe 1 and 2 have much more smooth profiles compared to probe 3 and 4. To quantitatively compare the profile smoothness of the four probes, we adopt a quantity called the total variation (Rudin *et al*., 1992) as defined by

$$V(P) = \sum_{x,y} \sqrt{\left|P_{x+1,y} - P_{x,y}\right|^2 + \left|P_{x,y+1} - P_{x,y}\right|^2}, \qquad (6)$$

where $V(P)$ is the total variation of probe P, and *xy* are the pixel indices along the two dimensions of the probe. The lower the number is, the less variation, i.e. more smooth, the probe profile is. The total variations for the four probes are calculated to be 0.96×10^3, 1.6×10^3, 2.4×10^3 and 5.0×10^3 respectively, which is consistent with the FRC comparison. Moreover, the oscillating nature of the FRCs at high frequencies from probe 3 and 4 also proves that the specimen reconstructions have unstable high frequencies.

2.3. The selected area setup

A microscope imaging system can be used to image the specimen onto an aperture (or an aperture plus a diffuser) which plays the role of the probe; when the sample is scanned, its image moves relative to the aperture. An illustration of the setup is shown in Fig. 7a. The aperture was set to have a diameter of 2.3mm, so that the probe formed at the specimen plane has a size of 107µm, to match the probe size of the previous experiments. The detector was placed at 250mm downstream of the aperture, where a well-developed diffraction pattern can cover most of the detector. Examples of the recorded diffraction patterns from probe 1 and probe 2 are respectively shown in Fig. 7b. As we mentioned above, plane wave illumination is preferred to form an image of the specimen, so only probe 1 and probe 2 are demonstrated for this setup.

The reconstruction was performed at the image plane, which means the object reconstruction needs to be demagnified by 21.45 to give the right scale. Again, according to the Fresnel number calculation (about 33.3, much bigger than 1), the reconstruction used the angular spectrum propagator for the propagation between the aperture plane and the detector plane. 200 iterations of ePIE were run on each data set with object initial guess being free space and probe initial guess being an aperture (for both the diffused and undiffused probes). The reconstructed probes (modulus part) and the reconstructed object (phase part) from probe 2 are respectively shown in Figs. 7c and 7d (the reconstructions are rescaled to the specimen plane). It should be noticed here that the object reconstructions are normally out-of-focused, due to the fact that the aperture was not exactly placed on the image plane. Therefore, an extra step of computational propagation is needed to bring the object reconstructions into focus. A zoom-in region of the in-focus object reconstructions are shown in Fig. 7e. Visually, the results are very good and comparable with that from the microscope setup. Likewise, FRC is calculated to quantitatively assess the image quality (see Fig. 8). Since the diffraction

patterns are also measured at the proximity of the specimen image plane, for the same reason described above in the microscope setup section, probe 1 produces better object reconstruction than probe 2.

3. DISCUSSIONS AND CONCLUSIONS

Here we have optically demonstrated ten ways to implement ptychography using three different setups. The comparisons have been conducted among each setup. Since we have used the same sample, an overall comparison of all the ten implementations using the FRC curves of the specimen reconstructions can be carried out and it is given in Fig. 9. The best reconstruction is produced by the pinhole probe in the microscope setup, while the worst reconstruction results from the pinhole probe in the lensless setup. Although this comparison is restricted to the specific experiments in this work, for the generic case, we can draw two inferences. First, it is preferable to spread the diffraction pattern using either a lens or a diffuser because this reduces the dynamic range of the data and therefore makes it easier to record. Second, a diverse data set (obtained by using a diffuser) better conditions the reconstruction problem, but this comes with the caveat that a highly speckled probe (i.e. one with a high total variation) can reduce the accuracy of the reconstruction, since here it is possible that some regions of the object may never be well illuminated by the probe.

For the lensless setup, the diffraction pattern is measured at a relatively large distance from the specimen, where Fresnel or Fourier propagation models can be used. In this case, the requirement on the dynamic range of the detector is high, so that the signals scattered to high angles can be measured with high fidelity against the noise. This is problematic for weakly scattering samples, but using a diffuser or a condenser lens can significantly improve the situation. The long working distance that the lensless setup allows is its principle benefit, it is also the simplest setup and the cheapest. These benefits are offset by practical considerations,

for instance the recorded diffraction patterns normally bear no relation to the profile of the specimen, so it is difficult to locate a region of interest, and accurate measurement of the distance from the specimen to the detector is a time consuming necessary step.

For the microscope setup, the diffraction pattern is measured at the vicinity of the virtual detector plane (i.e. the CCD conjugate plane, firmly in the near field). As a result, the dynamic range of the detector has only a minor influence on the reconstruction quality and the main limiting factor becomes the objective lens. When equipped with objectives of high quality and high NA, this setup produces good results just with a pinhole probe. But of course, good objectives are expensive. During the alignment, the specimen first coincides the virtual detector plane, so it is easy to locate the region of interest. Then, the specimen is defocused by moving the stage axially by a controllable distance, so the distance from the specimen to the measurement plane is known accurately. However, setting this distance too large reduces the NA of the system, so the working distance is quite limited.

For the selected area setup, the object reconstruction is the complex wave field in the selected area aperture plane. Only when the image plane coincides perfectly with the aperture plane is the specimen reconstruction in focus, otherwise a computational propagation is needed after the reconstruction to bring the specimen to focus. Since this setup compresses the specimen information into a 2D complex wave, it is very useful when the 3D scattering inside the specimen renders the multiplicative approximation on which the other methods rely inaccurate – an example of this is optical metrology for contact lenses or optics characterisation (Moore & Fienup, 2016).

For visible light, an advantage of the microscope setup is its compatibility with existing microscope platforms – a commercial microscope can be easily modified by adding a translational stage to implement ptychographic experiments. In this way, the resolution is still

determined by the transfer function of the imaging system, but quantitative phase images can be obtained.

For x-rays, the lensless setup becomes a routine way to obtain high resolution phase images. Zone plates are the predominant choice for the objective lens of high-resolution x-ray microscopes. However, the manufacture of narrow outer rings of a zone plate is very challenging and expensive, especially for hard x-rays. The lensless setup of ptychography not only removes the need for lenses and improves the resolution, but also gains the quantitative phase information. Our optical tests here confirm that the use of a diffuser in the probe-forming optics can be highly beneficial for x-ray ptychography (Maiden *et al*., 2014; Li *et al*., 2016; Stockmar *et al*., 2013). It is not practical to adopt the microscope setup and the selected area setup in the x-ray regime because of the poor quality and low numerical aperture of the zone plates.

For electrons, the lensless setup can be implemented on a scanning electron microscope, but a practical difficulty is adjustment of the magnification over a good range with a fixed or marginally adjustable camera length (Humphry *et al*., 2012). This is avoided by the use of the intermediate lenses in the transmission electron microscope, where the available options are the microscope setup (Putkunz *et al*., 2012) and the selected area setup (Maiden *et al*., 2015). Resolution improvements are not apparent in these two cases, where the primary gain is an effective way to quantify the phase of the electron wave. With recent developments, ptychography can also be implemented in scanning transmission electron microscopy (STEM) and provide quantitative phase information at atomic resolution (Yang *et al*., 2016).

4. ACKNOWLEDGEMENTS

5. REFERENCES

Bates, R. H. T. & Rodenburg, J. M. (1989) Sub-Ångström transmission microscopy: a Fourier transform algorithm for microdiffraction plane intensity infor-mation. *Ultramicroscopy* **31**, 303-307.

Brown, H. G., D'Alfonso, A. J., Chen, Z., *et al.* (2016) Structure retrieval with fast electrons using segmented detectors. *Phys. Rev. B* **93**, 134116.Dierolf, M., Menzel, A., Thibault, P., *et al.* (2010) Ptychographic X-ray computed tomography at the nanoscale. *Nature* **467**, 436-439.

Faulkner, H. M. L. & Rodenburg, J. M. (2004) Movable aperture lensless transmission microscopy: a novel phase retrieval algorithm. *Physical Review Letters* **93**, 023903.

Guizar-Sicairos, M. & Fienup, J. R. (2008) Phase retrieval with transverse translation diversity: a nonlinear optimization approach. *Optics Express* **16**, 7264-7278.

Godard, P., Carbone, G., Allain, M., *et al.* (2011) Three-dimensional high-resolution quantitative microscopy of extended crystals. *Nature Communications* **2**, 568.

Godden, T. M., Suman, R., Humphry, M. J., Rodenburg, J. M. & Maiden, A. M. (2014) Ptychographic microscope for three-dimensional imaging. *Optic Express* **22**, 12513-12523.

Goodman, J. W., (2005) Introduction to Fourier optics. Roberts and Company Publishers, 2005.

Hoppe, W. (1969) Diffraction in inhomogeneous primary wave fields. 1. Principle of phase determination from electron diffraction interference. *Acta Crystallogr. A* **25**, 495-501.

Hoppe, W. & Strube, G. (1969) Diffraction in inhomogeneous primary wave fields. 2. Optical experiments for phase determination of lattice interferences. *Acta Crystallogr. A* **25**, 502-507.

Hoppe, W. (1969) Diffraction in inhomogeneous primary wave fields. 3. Amplitude and phase determination for nonperiodic objects. *Acta Crystallogr. A* **25**, 508-515.

Hegerl, R. & Hoppe, W. (1970) Dynamische Theorie der Kristallstrukturanalyse durch Elektronenbeugung im inhomogen Primarstrahlwellenfeld. *Ber. Bunsenges. Physik. Chemie*. **74**, 1148-1154.

Hegerl, R. & Hoppe, W. (1972) Phase evaluation in generalized diffraction (ptychography). *Proc. Fifth Eur. Cong. Electron Microscopy*, 628-629.

Humphry, M. J., Kraus, B., Hurst, A.C., Maiden, A. M. & Rodenburg, J. M. (2012) Ptychographic electron microscopy using high-angle dark-field scattering for sub-nanometre resolution imaging. *Nature Communications* **3**, 730.

Li, P., Batey, D. J., Edo, T. B., Parsons, A. D., Rau, C. & Rodenburg, J. M. (2016) Multiple mode x-ray ptychography using a lens and a fixed diffuser optic. *Journal of Optics* **18**, 054008.

McCallum, B. C., Landauer, M. N. & Rodenburg, J.M. (1995) Complex image reconstruction of weak specimens from a three-sector detector in the STEM. *Optik*. **101**, 53–62.

Maiden, A. M. & Rodenburg, J. M. (2009) An improved ptychographical phase retrieval algorithm for diffractive imaging. *Ultramicroscopy* **109**, 1256-1262.

Maiden, A. M., Humphry, M. J., Sarahan, M. C., Kraus, B. & Rodenburg, J. M. (2012) An annealing algorithm to correct positioning errors in ptychogra-phy. *Ultramicroscopy* **120**, 64-72.

Maiden, A. M., Humphry, M. J. & Rodenburg, J. M. (2012) Ptychographic transmission microscopy in three dimensions using a multi-slice approach. *JOSA A* **29**, 1606-1614.

Maiden, A. M., Rodenburg, J. M. & Humphry, M. J. (2010) A new method of high resolution, quantitative phase scanning microscopy. *International Society for Optics and Photonics In Scanning Microscopy 2010*, 77291I-77291I.

Maiden, A. M., Sarahan, M. C., Stagg, M. D., Schramm, S. M. & Humphry, M. J. (2015) Quantitative electron phase imaging with high sensitivity and an unlimited field of view. *Scientific Reports* **5**, 14690.

Moore, D. B. & Fienup, J. R. (2016) Ptychography for optical metrology with limited translation knowledge. *Applied Optics* **55**, 4596-4610.

Maiden, A. M., Morrison, G. R., Kaulich B., Gianoncelli, A. & Rodenburg, J. M. (2014) Soft X-ray spectromicroscopy using ptychography with randomly phased illumination. *Nature communications* **4**, 1669.

Putkunz, C. T., D'Alfonso, A. J., Morgan, A. J., *et al.* (2012) Atom-scale ptychographic electron diffractive imaging of boron nitride cones. *Physical Review Letters* **108**, 073901.

Rodenburg, J. M. & Faulkner, H. M. (2004) A phase retrieval algorithm for shifting illumination. *Applied Physics Letters* **85**, 4795-4797.

Rudin, L. I., Osher, S. & Fatemi, E., (1992). Nonlinear total variation based noise removal algorithms. *Physica D*. **60**, 259–268.

Stockmar, M., Cloetens, P., Zanette, I., Enders, B., Dierolf, M., Pfeiffer, F. & Thibault, P. (2013) Near-field ptychography: phase retrieval for inline holography using a structured illumination. *Scientific Reports* **3**, 1927.

Thibault, P., Dierolf, M., Bunk, O., Menzel, A. & Pfeiffer, F. (2009) Probe retrieval in ptychographic coherent diffractive imaging. *Ultramicroscopy* **109**, 338-343.

Tripathi, A., McNulty, I. & Shpyrko, O. G. (2014) Ptychographic overlap constraint errors and the limits of their numerical recovery using conjugate gradient descent methods. *Optics Express* **22**, 1452-1466.

Thibault, P. & Menzel, A. (2013) Reconstructing state mixtures from diffraction measurements. *Nature* **494**, 68-71.

Thibault, P., Dierolf, M., Menzel, A., Bunk, O., David, C. & Pfeiffer, F. (2008) High-resolution scanning x-ray diffraction microscopy. *Science* **321**, 379-382.

Van Heel, M. & Schatz, M. (2005) Fourier shell correlation threshold criteria. *Journal of Structural Biology* **151**, 250-262.

Yang, H., Pennycook, T. J. & Nellist, P. D. (2015) Efficient phase contrast imaging in STEM using a pixelated detector. Part II: Optimisation of imaging conditions. *Ultramicroscopy* **151**, 232-239.

Yang. H, Rutte, R. N., Jones, L., *et al*. (2016) Simultaneous atomic-resolution electron ptychography and Z-contrast imaging of light and heavy elements in complex nanostructures. *Nature Communications* **7**, 12532.

Zhang, F., Peterson, I., Vila-Comamala, J., *et al*. (2013) Translation position determination in ptychographic coherent diffraction imaging. *Optics Express* **21**, 13592-13606.

Zheng, G., Horstmeyer, R. & Yang, C. (2013) Wide-field, high-resolution Fourier ptychographic microscopy. *Nature Photonics* **7**, 739-745.

Lay Description

Ptychography is a lensless imaging technique, able to routinely deliver quantitative phase images at diffraction limited resolution from a set of diffraction intensity measurements. There are three fundamental components: a confined coherent illumination, an overlapping scan strategy and an iterative image reconstruction algorithm. The confined illumination is scanned over the specimen at a grid of positions, such that the illuminated areas from two adjacent scan positions partially overlap (i.e. the overlapping scan). The transmitted (or reflected) wavefield is then captured by a camera located at somewhere downstream, but with the phase information of the wavefield lost. The overlapping scan generates redundancy in the measurements and the reconstruction algorithm allows us to utilize the redundancy to recover the phase information. Since no lens in involved during the whole imaging process, ptychography is able to bypass the resolution limits imposed by the poor lenses available at short wavelengths.

Although invented to circumvent the need for lenses, ptychography can also be implemented with their assistance. The confined illumination can be formed by: passing an extended beam through a pinhole or condensing the extended beam via a lens. In either way, a diffuser can be inserted to increase the angular range of the illumination, giving rise to the four probe-forming methods. For each probe, three imaging setups can be used to perform ptychography: lensless setup, microscope setup and selected area setup. Lensless setup means no lens is involved between the specimen and the camera. Microscope setup replaces the camera in the lensless setup with its demagnified version using a microscope imaging system (an objective lens and a tube lens). Selected area setup replaces the specimen in the lensless setup with its magnified image using the same imaging system.

Combined with the four probe types, the three imaging setups can give rise to ten ways to implement ptychography (since plane wave illumination is needed for the selected area setup, so probe with curved phase front, i.e. formed via a lens, cannot be used). Our objectives in this paper are to demonstrate these ten different configurations using visible light experiments, to compare their performance, and to assess the advantages and disadvantages of each approach.
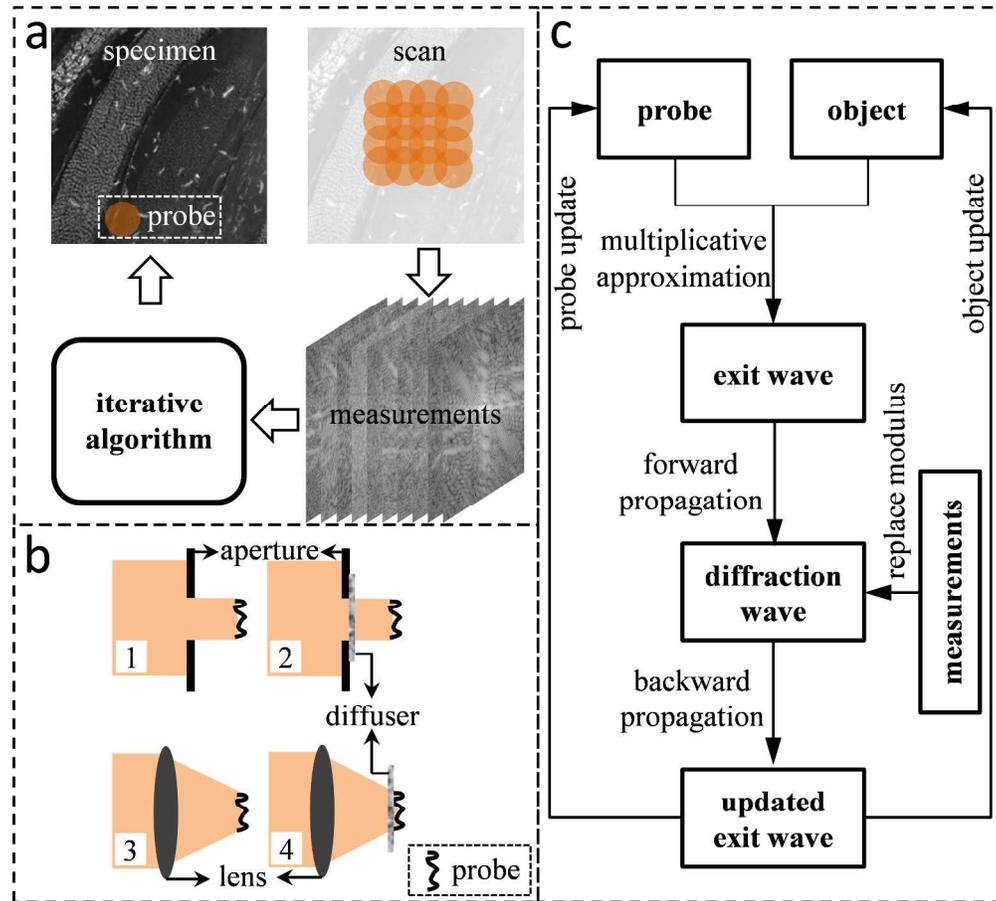
Figure 1. Ptychographic imaging. (a) The flow chart of ptychographic imaging. (b) The experimental geometries to form a localised probe in ptychography. (c) The block diagram of a typical iterative reconstruction algorithm in ptychography.

804x728mm (96 x 96 DPI)
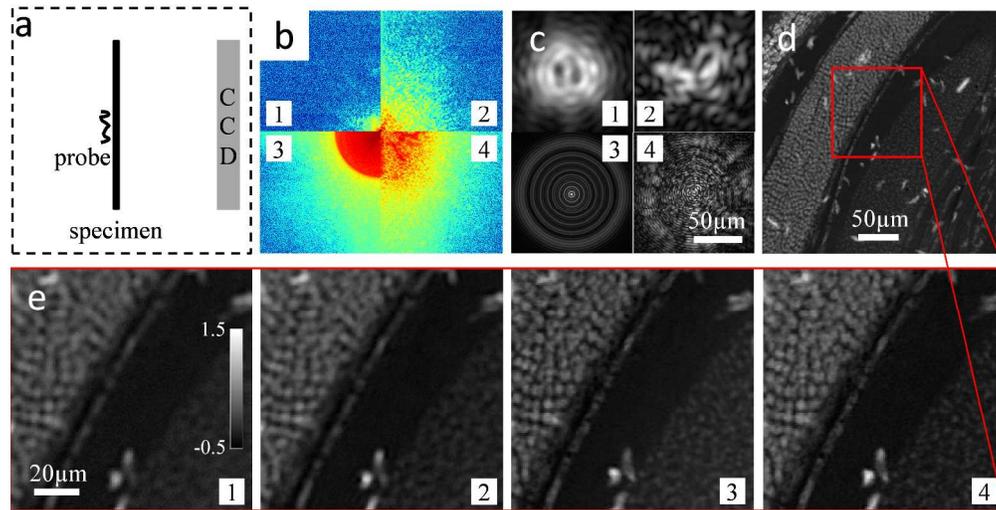
Figure 2. The lensless setup of ptychography. (a) Experimental configuration. The probe can be formed by any way of the four shown in Fig. 1b. (b) Example diffraction patterns from the four probe-forming optics. (c) The four probe reconstructions. (d) The phase part of the specimen reconstruction. (e) The zoom-ins of the specimen phase reconstructions from the four different probe-forming optics.

977x500mm (96 x 96 DPI)
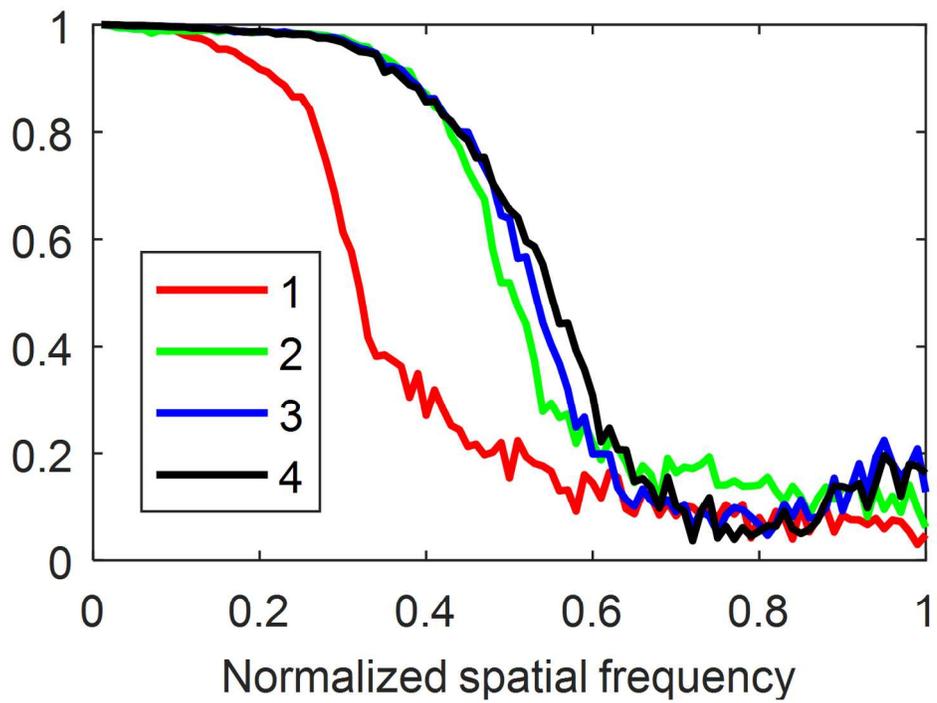
Figure 3. FRC curves comparison for the lensless setup

464x324mm (96 x 96 DPI)
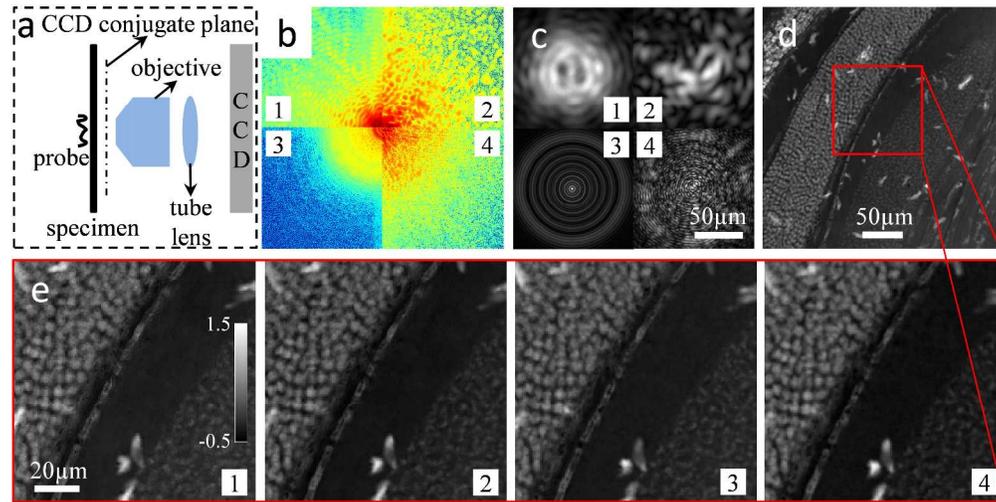
Figure 4. The microscope setup of ptychography. (a) Experimental configuration. The probe can be formed by any way of the four shown in Fig. 1b. (b) Example diffraction patterns from the four probe-forming optics. (c) The four probe reconstructions. (d) The phase part of the specimen reconstruction. (e) The zoom-ins of the specimen phase reconstructions from the four different probe-forming optics.

980x493mm (96 x 96 DPI)
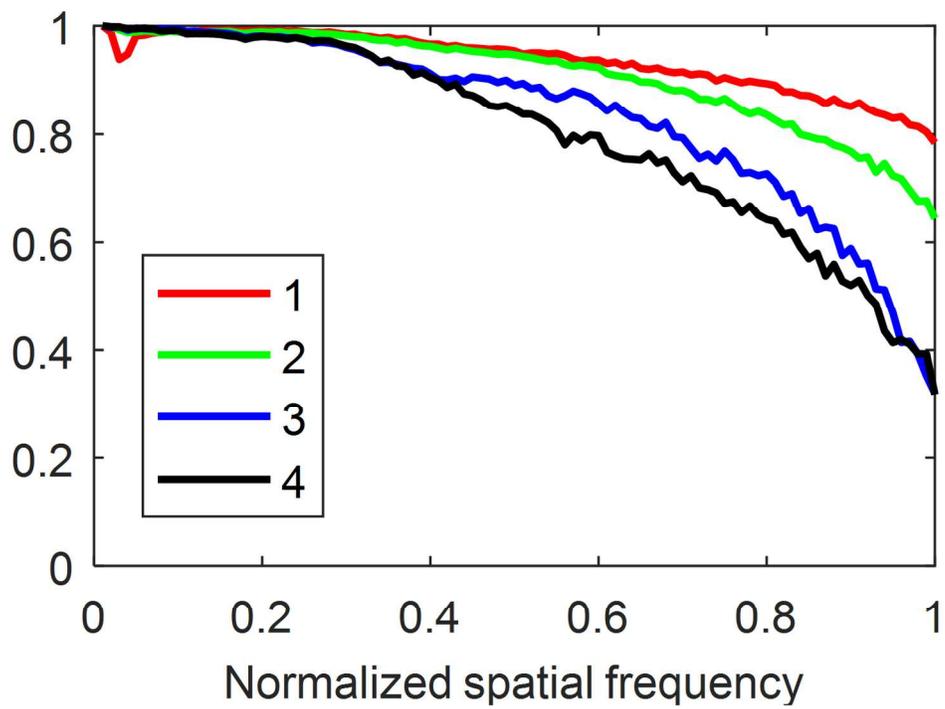
Figure 5. FRC curves comparison for the microscope setup

460x324mm (96 x 96 DPI)
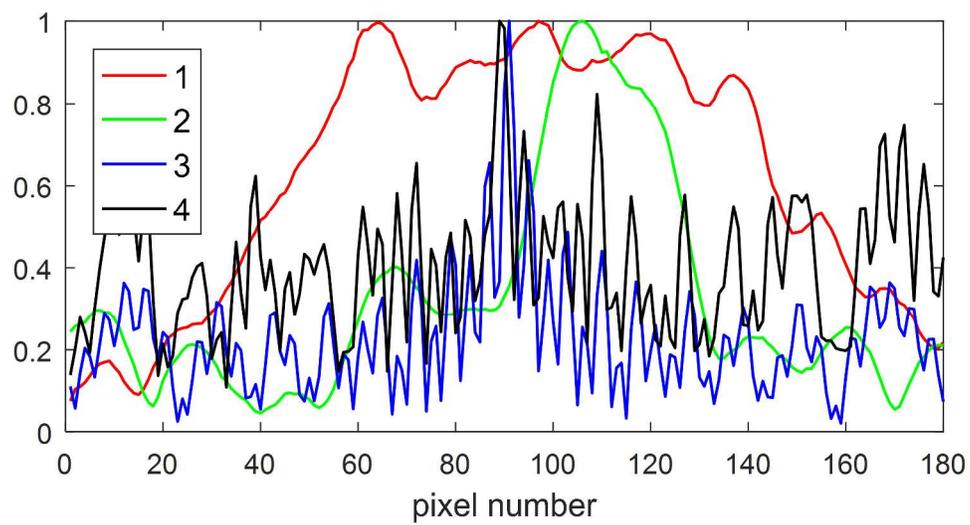
Figure 6. The cross-section plots of the four probes along the central vertical line.

802x420mm (96 x 96 DPI)
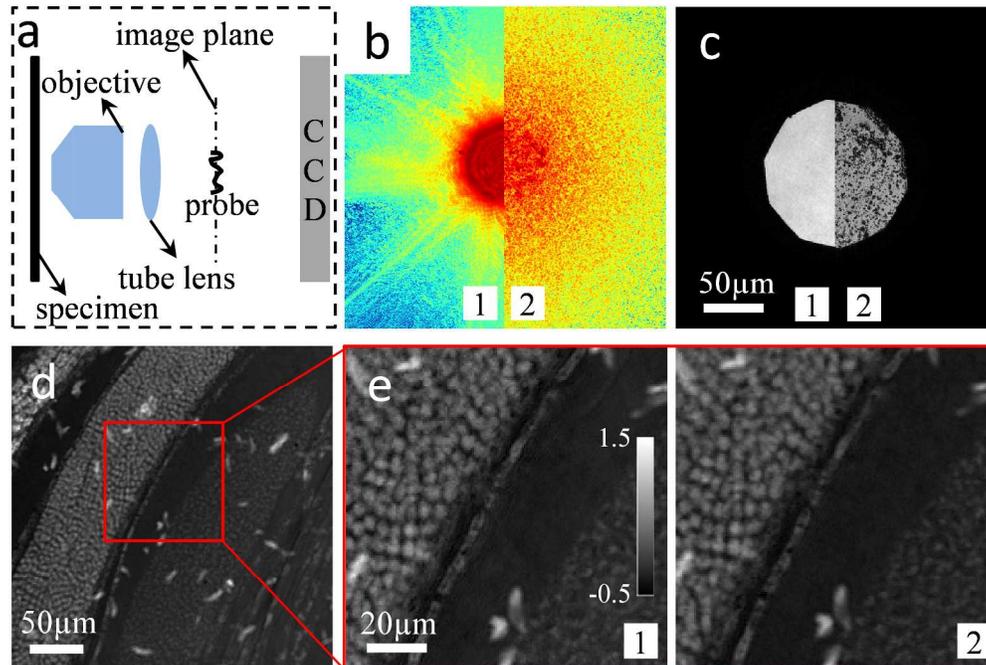
Figure 7. The selected area setup of ptychography. (a) Experimental configuration. The probe can only be formed by the first two ways shown in Fig. 1b. (b) Example diffraction patterns from the two probe-forming optics. (c) The two probe reconstructions. (d) The phase part of the specimen reconstruction. (e) The zoom-ins of the specimen phase reconstructions from the two probe-forming optics.

736x493mm (96 x 96 DPI)
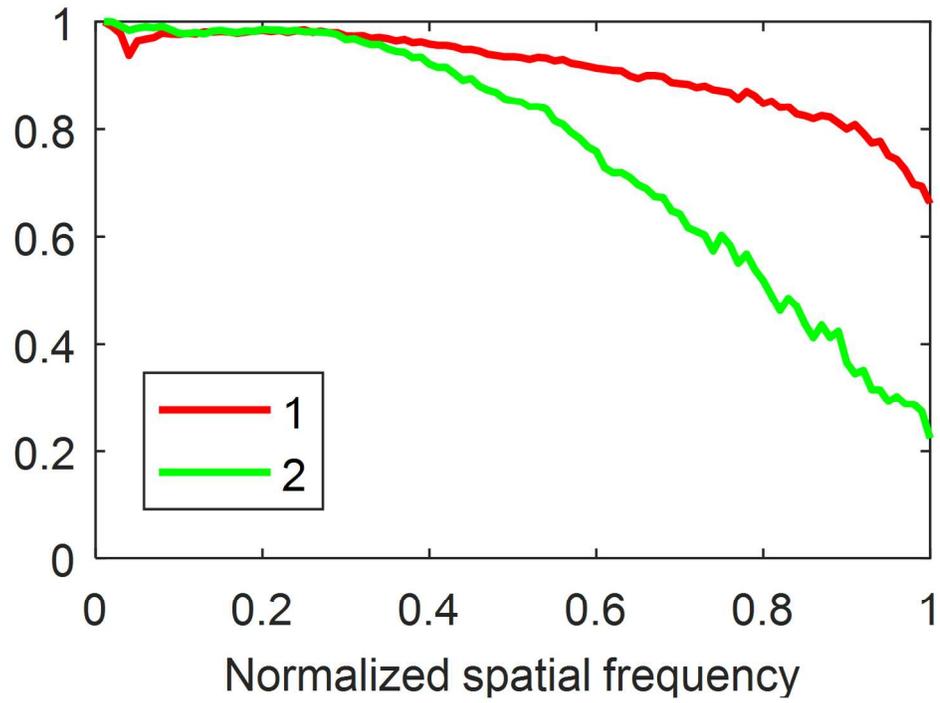
Figure 8. FRC curves comparison for selected area setup

463x323mm (96 x 96 DPI)
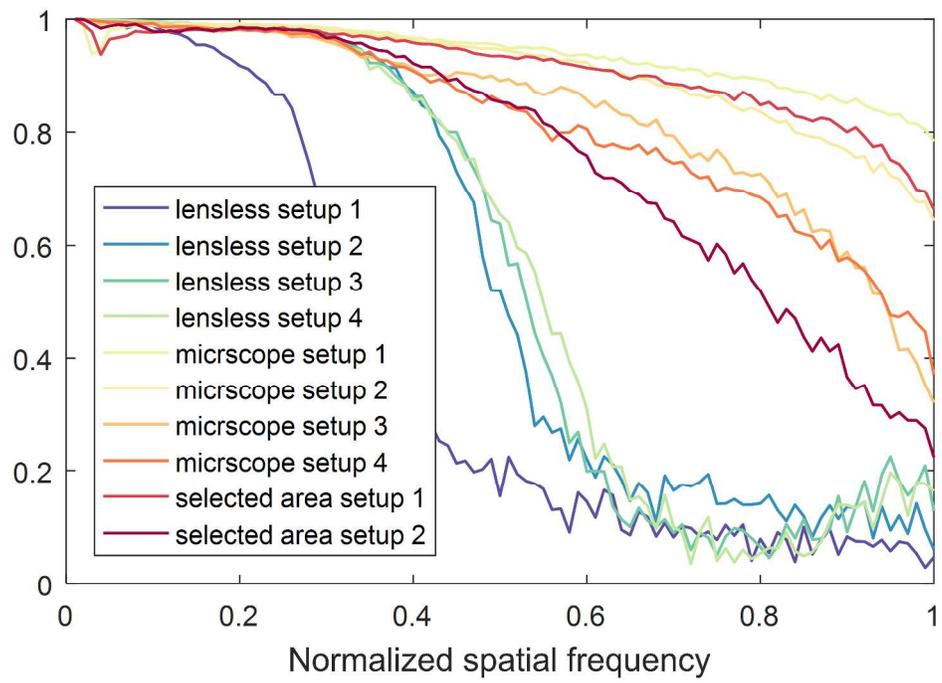
Figure 9. FRC curves comparison for all the ten implementations.

789x541mm (96 x 96 DPI)